Check for updates

NANO · MICRO small
www.small-journal.com

Non-Ultrawide Bandgap Semiconductor GaSe Nanobelts for Sensitive Deep Ultraviolet Light Photodetector Application

Chun-Yan Wu, Ming Wang, Jingyue Li, Yuxuan Le, Wu Fei, Ji-Gang Hu,* Di Wu, Yu-Xue Zhou, and Lin-Bao Luo**

In this paper, the authors report the fabrication of a sensitive deep ultraviolet (DUV) photodetector by using an individual GaSe nanobelt with a thickness of 52.1 nm, which presents the highest photoresponse at 265 nm illumination with a responsivity and photoconductive gain of about 663 A W^{-1} and 3103 at a 3 V bias, respectively, comparable to or even better than other reported devices based on conventional wide bandgap semiconductors. According to the simulation, this photoelectric property is associated with the wavelength-dependent absorption coefficient of the GaSe crystal, for which incident light with shorter wavelengths will be absorbed near the surface, while light with longer wavelengths will have a larger penetration depth, leading to a blueshift of the absorption edge with decreasing thickness. Further finite element method (FEM) simulation reveals that the relatively thin GaSe nanobelt exhibits an enhanced transversal standing wave pattern compared to its thicker counterpart at a wavelength of 265 nm, leading to an enhanced light–matter interaction and thereby more efficient photocurrent generation. The device can also function as an effective image sensor with acceptable spatial resolution. This work will shed light on the facile fabrication of a high-performance DUV photodetector from non-ultrawide bandgap semiconductors.

1. Introduction

Ultraviolet (UV) radiation, electromagnetic radiation with wavelengths ranging from ≈10 to 400 nm, constitutes ≈10% of the total solar spectrum.[1,2] Due to strong absorption by stratospheric ozone layers and the Earth's atmosphere, UV radiation with a wavelength shorter than 280 nm can hardly reach the Earth's surface.[3] Therefore, UV detection, in particular deep ultraviolet (DUV) detection, is characterized by relatively high detection precision and a lower false alarm ratio than its infrared and visible counterparts, which greatly facilitate its application in both civil and military fields, including ozone monitoring, flame detection, missile tracking and secure intersatellite communications.[4–9]

Currently, commercially available DUV photodetectors (e.g., photomultiplier tubes and Si photodetectors) normally operate at high bias voltage or adopt elaborate filters to eliminate the effect of visible and near infrared spectra.[10,11] To overcome the drawbacks of high power consumption as well as costly and complicated fabrication, a variety of ultrawide-bandgap (UWBG) semiconductors with bandgaps larger than 3.4 eV (the bandgap of GaN), such as $Al_xGa_{1-x}N$,[12] $Zn_xMg_{1-x}O$,[13] Ga_2O_3,[14] and diamond,[15] have been extensively explored. Various studies have shown that their relatively high radiation hardness and intrinsic visible blindness have indeed made them prominent candidates for highly sensitive DUV photodetection applications. However, to achieve good crystalline quality semiconductors, which is of vital importance for device performance, expensive apparatuses and intricate processes, such as plasma-enhanced chemical vapor deposition (PECVD),[16] molecular beam epitaxy (MBE)[17] and metal organic chemical vapor deposition (MOCVD),[18] are normally required, inevitably increasing the manufacturing cost of the DUV photodetectors. Moreover, the large barrier heights between UWBG semiconductors and metals make it difficult to realize reliable ohmic contact.[19] Therefore, development of a facile and effective strategy for DUV photodetection remains challenging.

In addition to the above UWBG semiconductor, two-dimensional (2D) layered semiconductor materials with a single layer

C.-Y. Wu, M. Wang, J. Li, Y. Le, L.-B. Luo
School of Microelectronics
Hefei University of Technology
Hefei 230009, China
E-mail: cywu@hfut.edu.cn; luolb@hfut.edu.cn
W. Fei, J.-G. Hu
School of Physics
Hefei University of Technology
Hefei 230009, China
E-mail: hujigang@hfut.edu.cn
D. Wu
School of Physics and Microelectronics
Zhengzhou University
Zhengzhou 450052, China
Y.-X. Zhou
College of Physical Science and Technology
Yangzhou University
Yangzhou 225002, China
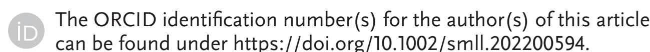
The ORCID identification number(s) for the author(s) of this article can be found under https://doi.org/10.1002/smll.202200594.

DOI: 10.1002/smll.202200594

 © 2022 Wiley-VCH GmbH

or few layers have also recently emerged as prominent candidates for achieving high-performance DUV photodetection due to their widened bandgap.[20,21] For example, the most studied MoS_2 exhibits a bandgap of 1.2 eV in bulk form and ≈1.8 eV in monolayer form.[22] Layer-dependent absorption has also been obtained in layered β-Te, and Guo et al. reported solar-blind DUV photodetection based on quasi 2D Te nanosheets (with a thickness of 18.9 nm), showing a responsivity and external quantum efficiency of 6.5×10^4 A W^{-1} and 2.26×10^6% at 261 nm.[23] On the other hand, very recently, various studies have shown that engineering the resonant field enhancements inside semiconductor nanostructures can adjust their spectral absorption, which opens up tremendous opportunities for the realization of DUV photodetection without the usage of UWBG semiconductors.[24] For example, by confining light within sub-wavelength, high-refractive-index semiconductor nanostructures, Brongersma et al. reported that the absorption peak of Ge nanowires can blueshift from 1250 to 600 nm by reducing their radius from 110 to 10 nm.[25] Due to the trapped electric field along the one-dimensional (1D) nanostructure by the excited TM01 resonant mode, ultrathin polymer nanofibrils (poly (3-hexylthiophene) poly (hexadecyloxyalene), P3HT-b-PHA) with an average diameter of ≈15 nm present highly sensitive solar-blind DUV photodetection.[26] Notably, spectral engineering strongly depends on the diameter of 1D semiconductor nanostructures, and a small diameter (sub-100 nm) is essential for DUV-sensitive photodetection.

Herein, we report a new DUV light photodetector fabricated by using CVD-grown GaSe nanobelts as building blocks. It was found that the device based on an individual 52.1 nm thick GaSe nanobelt displayed the highest photoresponse under 265 nm illumination, with a responsivity and gain of 663 A W^{-1} and 3103 at a 3 V bias, respectively. According to the theoretical simulation through Silvaco Technology Computer Aided Design (TCAD), this photoelectric property is associated with the wavelength-dependent absorption coefficient of the GaSe crystal,[27] for which a blueshift of the absorption edge was observed when the thickness of the GaSe crystal decreased. Further finite element method (FEM) simulations reveal that the thickness of the GaSe nanobelt is critical to selectively trap the incident light at the resonant wavelength, guaranteeing enhanced light–matter interaction for improved photoelectric response in the DUV region.

2. Results and Discussion

The operation of the proof-of-concept nanobelt DUV photodetector is based on the theory that illumination with different wavelengths on a semiconductor will cause sharp contrast in photoelectric properties. **Figure 1** shows the photon absorption in a GaSe crystal based on a Silvaco TCAD. It is clear that owing to the wavelength-dependent absorption coefficient of the GaSe crystal,[27] the photon absorption in the GaSe crystal varies for incident light with different wavelengths (Figure 1a–c). Specifically, the photon absorption rate for 265 nm incident light reaches $\approx 3.95 \times 10^{19}$ cm^3 s (Figure 1c) on the surface of the crystal due to the high absorption coefficient ($\approx 1.37 \times 10^5$ cm^{-1}, shown in Table S1, Supporting Information). Meanwhile, the incident light attenuates quickly when penetrating into the crystal (Figure 1d). According to the normalized attenuation curve of incident light (shown in Figure 1e), the penetration depth (defined as the distance where the energy of incident light is reduced to 1/e when it propagates in the medium)[28] for 265 nm incident light is deduced to be ≈42 nm. With increasing wavelength, the absorption coefficient decreases greatly, giving rise to a lower photon absorption rate on the surface and a larger penetration depth. For 660 nm incident light, the photon absorption is negligible and the attenuation of incident light power density is less than 20% within 1 μm. This is reasonable

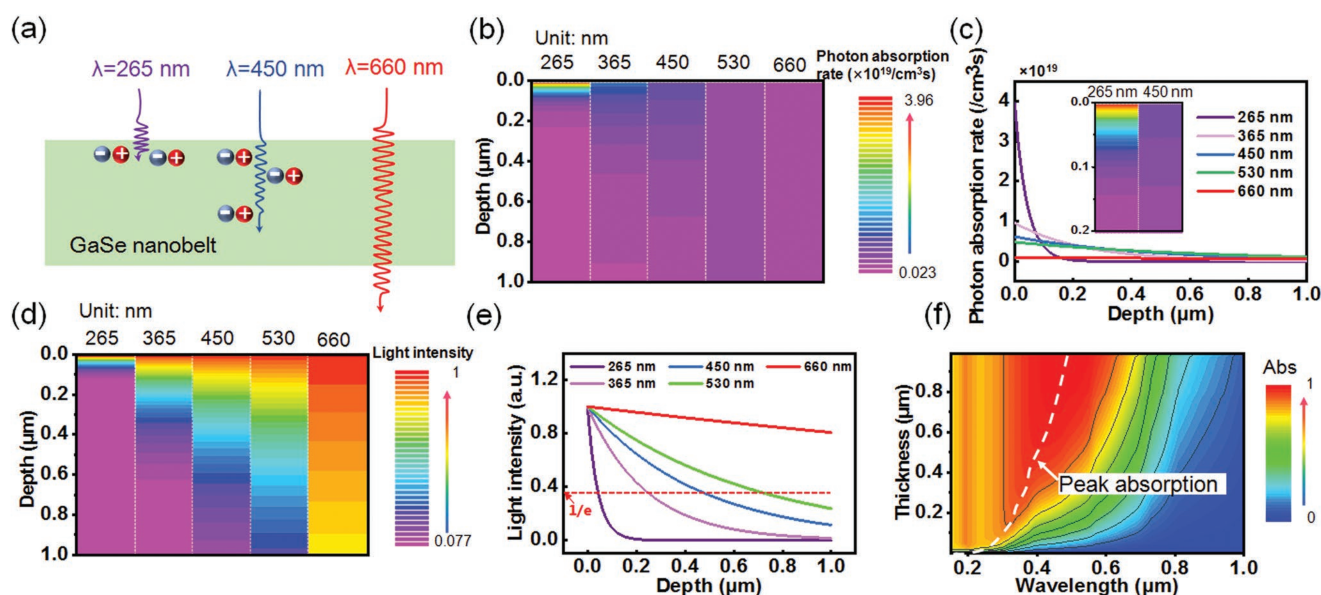

Figure 1. a) Schematic diagram of absorption in GaSe nanobelt for different wavelengths. b,c) Photon absorption rate versus depth, the inset shows the photon absorption in 200 nm-GaSe for 265 and 450 nm incident light. d) Attenuation of light power density versus depth and e) the normalized attenuation curve. f) Contour map of simulated absorption as a function of incident light wavelength and the thickness of nanobelt.

© 2022 Wiley-VCH GmbH

given that the photon energy is lower than the bandgap of bulk GaSe (≈2.1 eV). The simulated attenuation of power density is also consistent with the penetration depth calculated from the reported absorption coefficient (shown in Table S1, Supporting Information).[27] A higher photon absorption rate will bring about more photogenerated carriers in the semiconductor, leading to a higher photocurrent. In fact, the above thickness-dependent photoelectric characteristics were also confirmed by the theoretical simulation of the optical absorption for GaSe crystals with different thicknesses. As illustrated in the contour map shown in Figure 1f, the peak absorption of GaSe gradually blueshifts with decreasing thickness. The 1000 nm GaSe crystal is characterized by a peak absorption located at ≈490 nm, which blueshifts to ≈270 nm for the 50 nm thick GaSe, signifying the possibility of achieving DUV photodetection using ultrathin GaSe crystals by virtue of the wavelength-dependent penetration depth.

To verify the assumption mentioned above, several kinds of photodetectors were then assembled by using GaSe nanobelts with various thicknesses. The nanobelts were grown in a horizontal tube furnace by using a mixed source of GaSe and Ga_2Se_3, as illustrated in **Figure 2**a (more details can be found in the experimental section). Scanning electron microscopy (SEM) images of the as-obtained products are shown in Figure 2b, which present relatively uniform and flexible nanobelts with widths of 2–4 µm and lengths of up to hundreds of micrometers. Three remarkable diffraction peaks can be observed in the X-ray diffraction (XRD) pattern (Figure S2a, Supporting Information), which can be readily indexed to the (002), (004), and (006) crystallographic planes of hexagonal GaSe (JCPDS card no. 37-0931).[29] The XPS spectra (Figure S2b,c, Supporting Information) located at 19.6 and 54.7 eV can be well indexed to Ga 3d and Se 3d lines in GaSe, respectively.[30] The atomic ratio of Ga and Se is quantified to be 50.92:49.08, which is very close to the stoichiometric ratio of GaSe. What is more, according to the energy dispersive X-ray spectrum (EDS) in Figure S3 (Supporting Information), the elements Ga and Se are uniformly distributed in the elemental mapping of a typical nanobelt. High-resolution transmission electron microscopy (HRTEM) images taken from a single GaSe nanobelt (Figure 2c,d) and the corresponding selected area electron diffraction (SAED) (inset in Figure 2d) further verify the preferential orientation along the *c*-axis. This is also consistent with the layered structure of the GaSe crystal, which consists of vertically stacked covalently bonded Se-Ga-Ga-Se sheets held together by weak van der Waals forces (inset in Figure S2a, Supporting Information).[31] The Raman spectrum shows three prominent peaks at 131.9, 210.3, and 305.9 cm^{-1} (Figure 2e), corresponding to the A^1_{1g}, E^1_{2g}, and A^2_{1g} phonon vibrational modes of the GaSe crystal, respectively.[32] The intensity of the E^2_{1g} peak (located at 250.1 cm^{-1}) is relatively weak, suggesting the small thickness of the GaSe crystal.[33]

Figure 3a shows the schematic of a representative photodetector that is composed of a single GaSe nanobelt with a thickness of ≈52.1 nm (Figure 3b). The current–voltage (*I*–*V*) curves of the device in the dark and under illumination with different wavelengths are plotted in Figure 3c. Clearly, the device displays totally different photoresponses to illumination with various wavelengths of light: The photocurrent is the highest with an I_{on}/I_{off} ratio of 17.3 at 3 V upon 265 nm illumination. However, with increasing wavelength, the photocurrent gradually decreases, and the device is virtually blind to 660 nm illumination. Such a DUV sensitivity is understandable in that GaSe has a larger absorption coefficient and smaller penetration depth (≈42 nm, shown in Figure 1e) for 265 nm incident light, which means that most of the 265 nm light would be absorbed within the thickness of 52.1 nm. However, with increasing incident wavelength, the absorption coefficient of GaSe decreases, and the penetration depth increases accordingly. The attenuation of 450 nm incident light is only 10.7% for a thickness of 52.1 nm. In this case, the incident light would be partially absorbed, giving rise to a relatively low photocurrent. Although the DUV to visible rejection ratio R_{265}/R_{450} is not high (≈2.40) when compared to that of UWBG semiconductor based photodetectors (up to 10^3),[34] it presents an effective and facile strategy for DUV photodetection (Figure 3d). Figure 3e depicts the *I*–*V* curves of the photodetector under 265 nm illumination with various

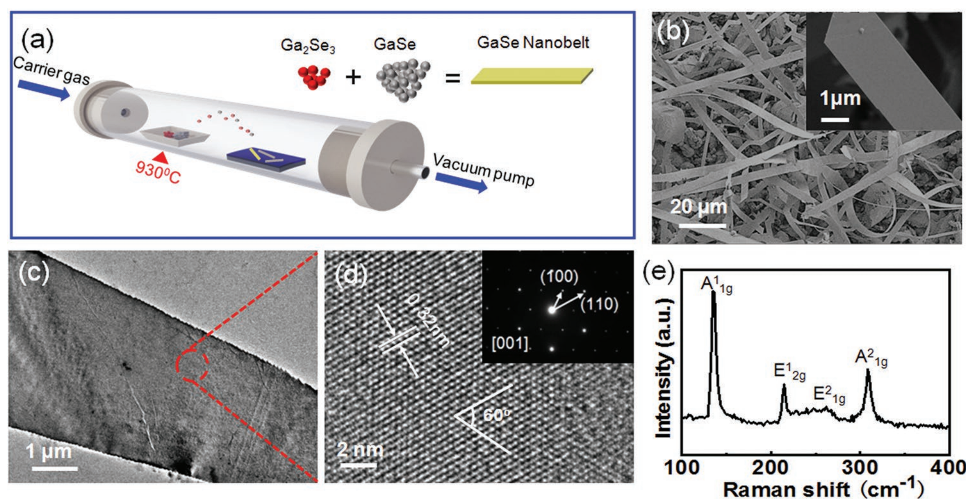

Figure 2. a) Schematic illustration for the synthesis of GaSe nanobelts. Characterization of the obtained GaSe nanobelts: b) SEM images, c) TEM image, and d) HRTEM image taken from the marked region in (c), the inset in (d) shows the corresponding SAED pattern. e) Raman spectrum.

© 2022 Wiley-VCH GmbH

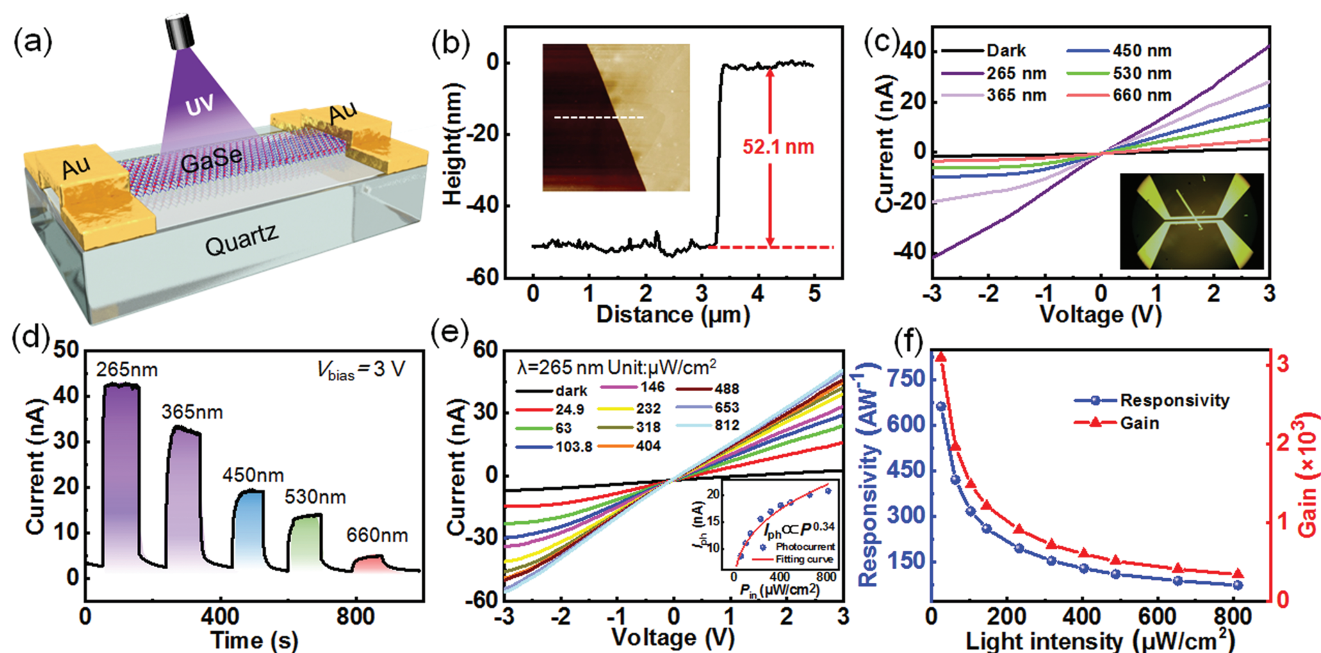

Figure 3. a) Schematic of the GaSe nanobelt DUV photodetector. b) Height profile of the GaSe nanobelt, the inset shows the AFM image. c) Current–voltage (*I*–*V*) curves of the photodetector in the dark and upon illumination with different wavelengths at the powder density of 0.31 mW cm^{-2}, the inset shows the optical image of a typical device. d) Time-dependent photoresponse of the device illuminated by incident light with various wavelengths at 3 V bias. e) *I*–*V* curves of the photodetector under 265 nm illumination with varied power density, the inset shows the photocurrent as a function of incident light power density. f) Responsivity and gain as a function of incident light power density upon 265 nm illumination.

light power density. It is clear that the photocurrent increases monotonically from 16.04 to 51.04 nA when the power density rises from 24.9 to 812 μW cm^{-2}. This is reasonable, as more electron–hole pairs will be generated upon light illumination with a stronger power density, leading to a higher photocurrent.[35] The dependence of the photocurrent on incident light power density was further fitted by using a general power law: $I_{ph} \propto p^{\theta}$, where I_{ph} is defined as the net photocurrent ($I_{ph} = I_{light} - I_{dark}$) and θ is an empirical value reflecting carrier recombination.[36] As plotted in the inset of Figure 3e, θ was defined to be 0.34, the deviation of which from the ideal value ($\theta = 1$) suggests the existence of recombination loss in the device.[37] This value was significantly higher than that of previously reported GaSe microbelts.[32] Meanwhile, the rise/fall time (τ_r/τ_f) of the device estimated from a single cycle is ≈0.44/3.24 s (Figure S4, Supporting Information). The recovery time is relatively faster than that of our previously reported GaSe microbelts with a spontaneously formed amorphous oxide (GaO_x) outer layer, revealing very good crystallinity.[32]

To quantitatively evaluate the performance of the GaSe nanobelt-based DUV photodetector, two key parameters, the responsivity (*R*) and photoconductive gain (*G*) of the device under 265 nm illumination with different light power density, were calculated by the following equations[38] and plotted in Figure 3f:

$$R = \frac{I_{light} - I_{dark}}{P_{in} S} \quad (1)$$

$$G = \frac{hcR}{\eta e \lambda} \quad (2)$$

where P_{in} is the incident light power density, *S* is the effective illuminated area of the device (defined as the area of the nanobelt between the two electrodes, ≈8.22 × 10^{-7} cm^2), *h* is the Planck constant, *c* is the velocity of light, *e* is the electronic charge, λ is the incident wavelength, and η is the internal quantum efficiency. By assuming 100% internal quantum efficiency, *R* and *G* reach the values of 663 A W^{-1} and 3103 at a 3 V bias under a power density of 24.9 μW cm^{-2}, respectively. Moreover, both parameters decrease with increasing power density. This is reasonable since more carriers are generated under the higher power density, leading to a higher recombination loss. The lowest NEP and the highest D^* are calculated to be 1.51×10^{-15} W Hz$^{-1/2}$ and 6.01×10^{11} Jones, respectively, demonstrating the ability to detect a weak light signal (Figure S5, Supporting Information). It is worth noting that the present GaSe nanobelt displays much better photoelectric performance than previously reported GaSe nanosheet, including mechanically exfoliated GaSe nanosheets[20,39] and gas-phase grown GaSe nanosheets,[40] which is comparable to or even better than that of traditional UWBG DUV photodetectors[12–15] (shown in **Table 1**), making it a promising candidate for application in future high-performance DUV photodetector-based devices and systems.

The optoelectronic characteristics of photodetectors based on GaSe with thicknesses of 36.3, 85.8, 351 nm, and microfilms (997 nm) were then studied (Figures S6–S9, Supporting Information) to verify the above theoretical prediction that the photoresponse of the nanodevice is thickness dependent. As can be seen from the normalized *I*–*T* curves (**Figure 4**a) and the corresponding rejection ratios R_{265}/R_{450} (Figure 4b), the devices exhibit different photorespones to incident light with different

© 2022 Wiley-VCH GmbH

Table 1. Comparison of key parameters of traditional DUV photodetectors and GaSe-based photodetectors.

Methods and materials	Measurement conditions	R [A W^{-1}]	Gain	D^* [Jones]	Ref.
CVD-grown GaSe nanobelt	265 nm@3 V	663	3.1×10^3	6.01×10^{11}	This work
MOCVD-grown AlGaN/GaN 2DEG[a)]	365 nm@−5 V	1670	5.24×10^5	–	[12]
VMT[b)]rown ZnMgO nanowires	254 nm@0.8 V	2.15×10^{-4}	1.05×10^3	2.17×10^{10}	[13]
CVD-grown Ga_2O_3 nanowires	365 nm@10 V	233	1×10^3	8.16×10^{12}	[14]
RIE[c)]tched diamond nanowires	350 nm@0 V	388	–	–	[15]
Mechanically exfoliated GaSe nanosheets	254 nm@5 V	2.8	13.67	–	[20]
VMT-grown GaSe nanosheets	405 nm@10 V	0.017	0.052	–	[40]
Mechanically exfoliated GaSe nanosheets	380 nm@5 V	2.6	8.5	5.46×10^{10}	[39]

[a)]Two-dimensional electron gas; [b)]Vapor phase mass transport; [c)]Reactive ion etching.

wavelengths. For instance, the 36.3 nm device shows the strongest photoresponse to 265 nm incident light with a rejection ratio R_{265}/R_{450} of ≈2.42, which decreases with increasing nanobelt thickness. However, according to the spectral response plotted in Figure 4c, the peak response of the devices is found to redshift with increasing thickness and reaches 530 nm for the 997 nm device, which is very close to the theoretical absorption edge of the bulk GaSe crystal. Such a redshift in the peak response is also consistent with the theoretical simulation of the optical absorption for GaSe crystals with different thicknesses (shown in Figure 1f), signifying its promise for application in DUV photodetection by reducing the thickness of non-UBWG semiconductors.

In addition to the wavelength-dependent light absorption that can result in selectivity in the light absorption spectrum and therefore the DUV photoresponse for thin GaSe nanobelts, another factor was also found to be important for the DUV photoresponse. **Figure 5**a–c shows the simulated |E| field intensity distributions in GaSe nanobelts with different thicknesses for 265 nm incident light (see the Experimental Section and Supporting Information for more details). Due to the larger absorption loss at the shorter wavelength,[27] light in the GaSe nanobelt displays interferential evanescent fields confined at the top. Compared with the thicker nanobelts, the |E| field intensity corresponding to the 50 nm-thick device exhibits an enhanced transversal standing wave pattern with a larger penetration depth in the nanobelt (Figure 5a). This consequently results in an enhanced light–matter interaction and thereby the highest photocurrent under 265 nm illumination (Figure 3d). As the thickness of the GaSe nanobelt increases up to 350 nm, a remarkable longitudinal Fabry–Pérot (F–P) cavity resonance can be observed, especially at a wavelength of 365 nm (Figure 5d–f), which provides an enhanced electric field with a larger mode volume in the nanobelt. The strong light–matter interaction in an enlarged area along the z-direction enables a resonant photocurrent near this wavelength, as shown in Figure S8c (Supporting Information). Similarly, as the thickness further increases to 1 µm, this longitudinal F–P resonance effect with remarkable field confinement in the nanobelt will redshift to the long wavelengths (Figure 5i). The resonance peak for the photocurrent response exhibits a corresponding redshift process, which is consistent with the thickness-dependent photoresponse of the GaSe nanobelt shown in Figure 4c. In light of the above, the thickness of the GaSe nanobelt is believed to be a critical parameter to

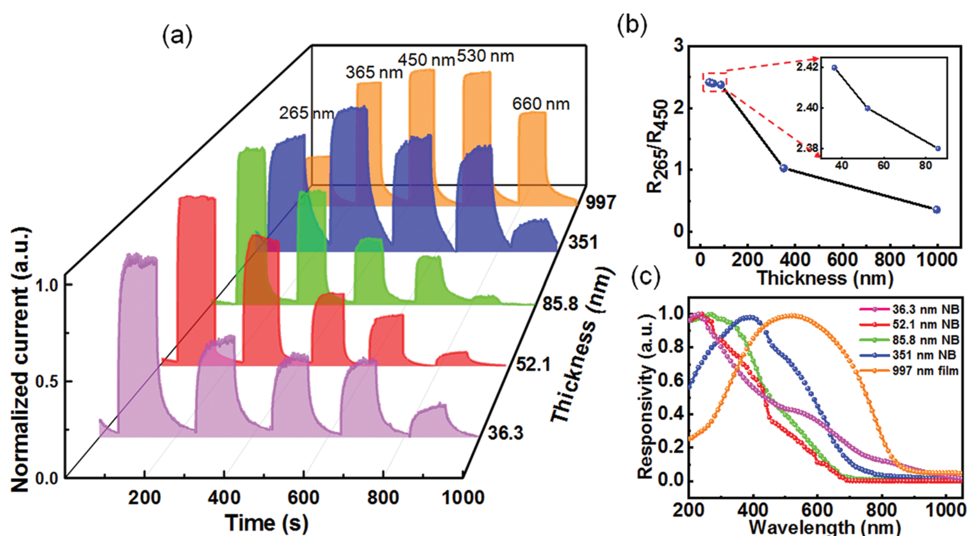

Figure 4. a) Normalized I–T curves under illumination with varied wavelengths, b) rejection ratios R_{265}/R_{450} and c) normalized photoresponse of devices based on nanobelts or microfilm with different thickness.

 © 2022 Wiley-VCH GmbH

Figure 5. Simulated |E| field intensity distributions in XOZ plane for 50 nm, 350 nm, and 1 µm GaSe nanobelts under the normal irradiation of plane wave at the wavelength of a–c) 265 nm, d–f) 365 nm, and g–i) 530 nm. Insets in (b) and (c) indicate the zoom-in |E| distributions for the top 25 nm.

selectively trap incident light at a specific resonant wavelength, offering an enhanced light–matter interaction for the improved photocurrent of the device. Clearly, the operation mechanism of our devices for DUV photodetection is totally different from that of the previously reported DUV photodetectors based on few layered GaSe nanosheets, which was ascribed to the 3.3 eV interband transition arising from the in-plane electronic states of p_x and p_y-like orbitals in the valence band of GaSe.[40–42]

Further study indicated that the present 52.1 nm-GaSe nanobelt photodetector can work as a DUV sensor that can record a DUV image with acceptable resolution. As illustrated in **Figure 6**a, a lab-made shadow mask with an open "UV" pattern (8 mm × 12 mm) was placed between the light source and the photodetector, which was fixed on a platform driven by a stepper motor and driven to progressively scan horizontally (X-axis) and vertically (Y-axis) at a step length of 0.25 mm. The photocurrent at each position was recorded and integrated into a 2D current mapping. As we can see from Figure 6b, the "UV" pattern can be clearly identified with a reasonable spatial resolution when illuminated by 265 nm incident light. This suggests the possibility of applying the 52.1 nm GaSe nanobelt-based photodetector in future DUV optoelectronic systems.

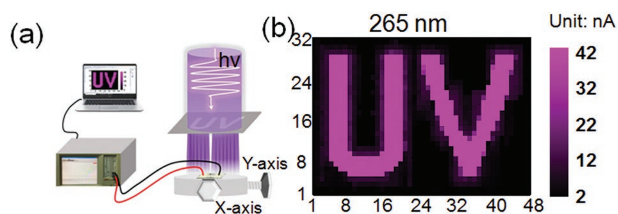

Figure 6. a) Schematic illustration of the DUV imaging system. b) 2D current mapping upon 265 nm illumination of the 52.1 nm GaSe nanobelt-based device.

3. Conclusion

In conclusion, we have reported the fabrication of a sensitive DUV photodetector by using a non-UWBG semiconductor nanobelt as a building block. Due to the wavelength-dependent absorption coefficient of GaSe, incident photons with shorter wavelengths are absorbed on the superficial surface, while longer wavelength light has a larger penetration depth. This leads to a blueshift of the peak absorption for the GaSe nanobelt with decreasing thickness. Theoretical simulation verifies that the thickness of the GaSe nanobelt is of paramount importance to achieve wavelength-selective field localization. The 50 nm GaSe nanobelt exhibits an enhanced transversal standing wave pattern compared to its thicker counterpart at a wavelength of 265 nm, resulting in enhanced light–matter interactions and

 © 2022 Wiley-VCH GmbH

thereby more efficient photocurrent generation. Experimental analysis reveals that the device made of a single 52.1 nm-GaSe nanobelt indeed displays a prominent photoresponse to DUV illumination, with responsivity and gain of ≈663 A W^{-1} and 3103 at a 3 V bias, respectively. Moreover, the GaSe nanobelt device can also function as a DUV image sensor with acceptable resolution. This work suggests that non-UWBG semiconductor nanostructures are potential candidates for the assembly of DUV photodetectors in the future.

4. Experimental Section

Materials Preparation and Characterization: The growth of GaSe nanobelt s was performed in a horizontal tube furnace through a chemical vapor deposition (CVD) method. In a typical process, a mixture of high-purity GaSe and Ga_2Se_3 (57.1 mg: 2.9 mg, molar ratio 50:1) powder was loaded into an alumina boat and then placed in the center region of the furnace. The cleaned silicon substrate was placed at the downstream position ≈15 cm from the mixed powder source. The system was first evacuated to a base pressure of 1×10^{-3} Pa and then filled with a constant Ar gas flow of 20 sccm to a chamber pressure of about 250 Pa. The source was heated to 930 °C and maintained at that temperature for 20 min, followed by a natural cooling to room temperature. A layer of gray fluffy products can be observed on the substrate.

The morphologies and structures of the obtained GaSe nanobelts were characterized by X-ray diffraction (XRD, X'Pert PRO MPD), scanning electron microscopy (SEM, JEOL JEM-2100F), high-resolution transmission electron microscopy (HRTEM, JEM-2100F) and atomic force microscopy (AFM, Dimension Icon). The chemical composition of GaSe nanobelts was studied by X-ray photoelectron spectrometer (XPS, Thermo, ESCALAB250Xi) and energy-dispersive X-ray spectroscopy (EDS, Oxford INCA, attached to HRTEM). Raman scattering spectrum was carried on laser confocal Raman spectrometer (Lab RAM HR Evolution) equipped with 532 nm laser for excitation.

Device Fabrication and Characterization: For the fabrication of GaSe nanobelts photodetector, parallel Au electrodes (50 nm) were defined on both ends of a single GaSe nanobelt through UV photolithography, electron beam evaporation and a subsequent lift-off process, forming the channel with a length of 10 µm. Optoelectronic properties of the device were characterized under ambient conditions at room temperature by using a semiconductor characterization system (Keithley 4200-SCS) equipped with a broadband monochromator (LE-SP-M300). Laser diodes with different wavelengths (Thorlabs, 265–1050 nm) were used as illumination sources, whose power density were calibrated by a power meter (Thorlabs GmbH, PM 100D) before measurement.

Theoretical Simulation: The photon absorption of the GaSe was simulated by using the 2D optoelectronic simulator Luminous of Silvaco Technology Computer Aided Design (TCAD). Ray tracing was chosen to describe the propagation of light, using the calculated refractive index and extinction coefficient along the crystallographic *c*-direction of GaSe crystals.[27] An optical beam with the light power density of 0.126 mW cm^{-2} and the incident angle of 90° was modeled as a collimated source for the simulation to match the experiments. To ensure the accuracy of the calculation results, the mesh grids along Y axis were set to increase from 1.5 to 5 nm uniformly within the depth of 85 nm, which was then increased to 10 nm during the depth of 85–350 nm. The mesh grids were set to be 10 nm for the rest depth to compromise the precision and the calculation time. Moreover, the Shockley–Read–Hall statistics (SRH) was adopted for the generation–recombination model and optical recombination (OPTR) was adopted for the radiative recombination model.

To gain a physical insight into the enhanced photoelectric response in the ultra-thin GaSe nanobelt, finite element method (FEM) was employed to calculate electrical field distribution of the structure. Structural parameters of the model were extracted from the SEM image of the experimental sample, which were the width of GaSe nanobelt W = 8 µm and the thickness t = 50 nm, 350 nm, and 1 µm, respectively. The refractive index of anisotropic GaSe was chosen from ref. [27] and that of substrate (SiO_2) was set as 1.43. Scattering boundary conditions were applied in horizontal direction to simulate an infinite area in the X and Y directions, and the perfectly matched layer (PML) boundary conditions were set on the top/bottom sides. In order to ensure the accuracy of the calculation results, the spatial mesh grids were set as ΔX = 10 nm and ΔZ = 10 nm. The structure was normally illuminated by a plane wave with its polarization along the *y*-direction.

Supporting Information

Supporting Information is available from the Wiley Online Library or from the author.

Acknowledgements

This work was supported by the National Natural Science Foundation of China (Nos. 62074048, 62075053, 92050202, and U20A20216), the Key Research and Development Plan of Anhui Province and the Fundamental Research Funds for the Central Universities (PA2020GDKC0014, PA2020GDKC0024, JZ2018HGXC0001).

Conflict of Interest

The authors declare no conflict of interest.

Data Availability Statement

Data sharing is not applicable to this article as no new data were created or analyzed in this study.

Keywords

deep ultraviolet (DUV) photodetectors, GaSe nanobelts, non-ultrawide bandgap semiconductors, penetration depth

Received: January 27, 2022
Revised: April 19, 2022
Published online: May 13, 2022

[1] P. E. Glaser, *Science* **1968**, *162*, 857.
[2] H. Chen, K. Liu, L. Hu, A. A. Al-Ghamdi, X. Fang, *Mater. Today* **2015**, *18*, 493.
[3] H. Chen, P. Yu, Z. Zhang, F. Teng, L. Zheng, K. Hu, X. Fang, *Small* **2016**, *12*, 5809.
[4] C. Xie, X.-T. Lu, X.-W. Tong, Z.-X. Zhang, F.-X. Liang, L. Liang, L.-B. Luo, Y.-C. Wu, *Adv. Funct. Mater.* **2019**, *29*, 1806006.
[5] X. Sheng, C. Yu, V. Malyarchuk, Y.-H. Lee, S. Kim, T. Kim, L. Shen, C. Horng, J. Lutz, N. C. Giebink, J. Park, J. A. Rogers, *Adv. Opt. Mater.* **2014**, *2*, 314.
[6] B. Zhao, F. Wang, H. Chen, L. Zheng, L. Su, D. Zhao, X. Fang, *Adv. Funct. Mater.* **2017**, *27*, 1700264.
[7] T. Oishi, N. Kawano, S. Masuya, M. Kasu, *IEEE Electron Device Lett.* **2017**, *38*, 87.
[8] R. Zou, Z. Zhang, Q. Liu, J. Hu, L. Sang, M. Liao, W. Zhang, *Small* **2014**, *10*, 1848.

© 2022 Wiley-VCH GmbH

[9] J. Lu, X. Sheng, G. Tong, Z. Yu, X. Sun, L. Yu, X. Xu, J. Wang, J. Xu, Y. Shi, K. Chen, *Adv. Mater.* **2017**, *29*, 1700400.
[10] J. Xing, K. Zhao, H. B. Lu, X. Wang, G. Z. Liu, K. J. Jin, M. He, C. C. Wang, G. Z. Yang, *Opt. Lett.* **2007**, *32*, 2526.
[11] S. Mitra, Y. Pak, N. Alaal, M. N. Hedhili, D. R. Almalawi, N. Alwadai, K. Loganathan, Y. Kumarasan, N. Lim, G. Y. Jung, I. S. Roqan, *Adv. Opt. Mater.* **2019**, *7*, 1900801.
[12] Y. Y. Zhang, Y. X. Zheng, J. Y. Lai, J. H. Seo, K. H. Lee, C. S. Tan, S. An, S. H. Shin, B. Son, M. Kim, *ACS Nano* **2021**, *15*, 8386.
[13] E. A. Azhar, J. Vanjaria, S. Ahn, T. Fou, S. K. Dey, T. Salagaj, N. Sbrockey, G. S. Tompa, H. Yu, *ACS Omega* **2018**, *3*, 4899.
[14] C. Xie, X. T. Lu, M. R. Ma, X. W. Tong, Z. X. Zhang, L. Wang, C. Y. Wu, W. H. Yang, L. B. Luo, *Adv. Opt. Mater.* **2019**, *7*, 1901257.
[15] A. F. Zhou, R. Velazquez, X. Wang, P. X. Feng, *ACS Appl. Mater. Interfaces* **2019**, *11*, 38068.
[16] P. Xing, D. Ma, K. J. A. Ooi, J. W. Choi, A. M. Agarwal, D. Tan, *ACS Photonics* **2019**, *6*, 1162.
[17] J. Kamimura, P. Bogdanoff, M. Ramsteiner, P. Corfdir, F. Feix, L. Geelhaar, H. Riechert, *Nano Lett.* **2017**, *17*, 1529.
[18] Z. J. Liu, T. Huang, J. Ma, C. Liu, K. M. Lau, *IEEE Electron Device Lett.* **2014**, *35*, 330.
[19] A. M. Armstrong, A. A. Allerman, *Appl. Phys. Lett.* **2016**, *109*, 222101.
[20] P. Hu, Z. Wen, L. Wang, P. Tan, K. Xiao, *ACS Nano* **2012**, *6*, 5988.
[21] M. Houssa, A. Dimoulas, A. Molle, *2D Materials for Nanoelectronics*, CRC Press, Boca Raton **2016**.
[22] S. Das, H. Y. Chen, A. V. Penumatcha, J. Appenzeller, *Nano Lett.* **2013**, *13*, 100.
[23] R. Cao, Y. Zhang, H. Wang, Y. Zeng, J. Zhao, L. Zhang, J. Li, F. Meng, Z. Shi, D. Fan, Z. Guo, *Nanophotonics* **2020**, *9*, 2459.
[24] L. Cao, P. Fan, A. P. Vasudev, J. S. White, Z. Yu, W. Cai, J. A. Schuller, A. Fan, M. K. Brongersma, *Nano Lett.* **2010**, *10*, 439.
[25] L. Cao, J. S. White, J. S. Park, J. A. Schuller, B. M. Clemens, M. L. Brongersma, *Nat. Mater.* **2009**, *8*, 643.
[26] L. Z. Qiu, S. Y. Wei, H. S. Xu, Z. X. Zhang, Z. Y. Guo, X. G. Chen, S. Y. Liu, D. Wu, L. B. Luo, *Nano Lett.* **2020**, *20*, 644.
[27] S.-R. Zhang, S.-F. Zhu, B.-J. Zhao, L.-H. Xie, K.-H. Song, *Physica B* **2014**, *436*, 188.
[28] C. Chen, F. Mou, L. Xu, S. Wang, J. Guan, Z. Feng, Q. Wang, L. Kong, W. Li, J. Wang, Q. Zhang, *Adv. Mater.* **2017**, *29*, 1603374.
[29] Y. Ni, H. Wu, C. Huang, M. Mao, Z. Wang, X. Cheng, *J. Cryst. Growth* **2013**, *381*, 10.
[30] H. Iwakuro, C. Tatsuyama, S. Ichimura, *Jpn. J. Appl. Phys.* **1982**, *21*, 94.
[31] D. J. Late, B. Liu, J. Luo, A. Yan, H. S. S. R. Matte, M. Grayson, C. N. R. Rao, V. P. Dravid, *Adv. Mater.* **2012**, *24*, 3549.
[32] C. Y. Wu, H. Zhu, M. Wang, J. Kang, C. Xie, L. Wang, L. B. Luo, *J. Mater. Chem. C* **2020**, *8*, 5375.
[33] D. J. Late, B. Liu, H. S. S. R. Matte, C. N. R. Rao, V. P. Dravid, *Adv. Funct. Mater.* **2012**, *22*, 1894.
[34] W. Song, J. Chen, Z. Li, X. Fang, *Adv. Mater.* **2012**, *33*, 2101059.
[35] H. Arora, R. Dong, T. Venanzi, J. Zscharschuch, H. Schneider, M. Helm, X. Feng, E. Canovas, A. Erbe, *Adv. Mater.* **2020**, *32*, 1907063.
[36] N. Joshi, *Photoconductivity: Art: Science & Technology*, CRC Press, Boca Raton **1990**.
[37] L. Wang, J. Jie, Z. Shao, Q. Zhang, X. Zhang, Y. Wang, Z. Sun, S. T. Lee, *Adv. Funct. Mater.* **2015**, *25*, 2910.
[38] J. M. Liu, *Photonic Devices*, Cambridge University Press, Cambridge **2009**.
[39] S. Sorifi, M. Moun, S. Kaushik, R. Singh, *ACS Appl. Electron. Mater.* **2020**, *2*, 670.
[40] S. Lei, L. Ge, Z. Liu, S. Najmaei, G. Shi, G. You, J. Lou, R. Vajtai, P. M. Ajayan, *Nano Lett.* **2013**, *13*, 2777.
[41] L. Plucinski, R. L. Johnson, B. J. Kowalski, K. Kopalko, B. A. Orlowski, Z. D. Kovalyuk, G. V. Lashkarev, *Phys. Rev. B* **2003**, *68*, 125304.
[42] A. Segura, J. Bouvier, M. V. Andrés, F. J. Manjon, V. Munoz, *Phys. Rev. B* **1997**, *56*, 4075.

© 2022 Wiley-VCH GmbH